Process parameter optimization of laser additive manufactured AlCrFeNiTiVZr alloys using response surface technique

Abidemi. Adeyoye[1,*], *Patricia* Popoola[1], *Olawale* Popoola[2], *Samson* Adeosun[1], *Shamaine* Makinita[1] and *Modupeola* Dada

[1]* Department of Chemical, Metallurgical and Materials Engineering, Tshwane University of Technology, South Africa

[2]Center for Energy and Electric power, Electrical Engineering, Faculty of Engineering and Built Environment, Tshwane University of Technology, Pretoria

Abstract. This study investigates the effect of laser power on the mechanical properties of equiatomic AlCrFeNiTiVZr high entropy alloy (HEA) fabricated using the Laser Additive Manufacturing (LAM) process. Laser powers of 300, 320, 340, 360, and 380 W were varied, while the scanning speed was held constant at 6.73 mm/s. The analyzed key performance indicators include microstructure, nanohardness, elastic modulus, and wear resistance. A combination of experimental evaluation and statistical modeling using design of experiments (DOE) and analysis of variance (ANOVA) was employed to identify optimal mechanical and tribological responses and to assess the relationships between laser parameters and alloy performance. The results indicate that higher laser power is crucial in achieving microstructural characteristics, which leads to a balance of hardness, strength properties and wear resistance. Predictions from the developed models suggest that the optimal power input should be within the range of 340–380 W. The validation process showed that the variation between what the models predicted and the actual experimental results is less than 0.05, confirming that the models are reliable for future predictions.

Key words: High entropy alloys (HEAs), AlCrFeNiTiVZr Alloy, Laser Additive Manufacturing (LAM), Process Parameter Optimization, Direct Energy Deposition (DED), Response Surface Methodology (RSM, Analysis of Variance (ANOVA), Statistical Modeling, Design of Experiments (DoE), Mechanical properties

* Corresponding author: abidemiadeyoye@gmail.com

1 Introduction

High-Entropy Alloys (HEAs) are of great interest to researchers due to their exceptional thermodynamic, kinectic, and structural stability, coupled with outstanding mechanical properties [1-3]. These attributes are primarily governed by the "four core effects" namely high mixing entropy, severe lattice distortion, sluggish diffusion, and cocktail effect [4-5]. As a result, HEAs demonstrate superior hardness and strength, outstanding resistance to oxidation and corrosion, remarkable thermal stability, and enhanced wear resistance, making them viable options for various industrial applications. However, challenges remain in accurately predicting and controlling their phase formation, optimizing their microstructural characteristics, and efficiently exploring the process design space, which has hindered their broader adoption [6-7]. Therefore, there is a pressing need for the development of effective and efficient techniques to produce this innovative class of alloys.

Additive Manufacturing (AM), particularly laser-based techniques, has emerged as a viable approach for fabricating HEAs as advanced engineering materials [8-9]. AM technologies, often referred to as 3D printing or Rapid Prototyping (RP), have advanced significantly in recent decades because of their ability to directly create 3D items stepwise with nearly net-shaping proportions using a Computer-Aided Design (CAD) model. In 2013, Kunce *et al*. [10] conducted the first study on additively made HEAs and since then, the volume of publications on this subject has grown dramatically during the past 10 years, particularly since 2019. AM provides significant advantages such as rapid and controlled cooling rates and the capacity to produce complex geometries that are often unachievable through traditional manufacturing methods, all without the need for molds or specialized tooling [11-12]. However, these benefits are sometimes offset by inherent limitations, such as material shrinkage and the development of residual stresses, which can affect dimensional accuracy and mechanical performance [13-15]. The extent of these issues is strongly influenced by the interplay between laser processing parameters and material behavior. Inadequate control of parameters such as laser power, scan speed, and heat input can exacerbate thermal gradients, leading to distortion, cracking, or inconsistency in part quality. Therefore, optimizing key operational parameters, particularly scanning speed, powder feed rate, and laser power is essential for achieving reliable mechanical performance in laser-processed HEAs [16-17]. The optimization challenge is compounded by the nonlinear interactions between processing variables and the multi-component nature of HEAs [18]. The compositional complexity of HEAs adds another level of difficulty, as it influences the processing conditions affecting microstructure and mechanical properties. Therefore, understanding and modeling the interrelationships among process parameters and material responses, such as mechanical strength and wear resistance, are critical concerns for maximizing the performance of laser-processed HEAs [19-20].

To this end, several studies have employed Response Surface Methodology (RSM), which is a statistical technique that models and optimizes processes involving multiple variables. RSM provides a structured approach to investigate the influence of laser parameters on performance metrics and to identify optimal settings [21-24]. Dong *et al*. [25] applied RSM to optimize scanning speed, powder feed rate, and laser power for $AlCoCrFeNi_{2.1}$ coatings produced via laser cladding. The study achieved a microhardness value of 322.70 HV0.2 under laser operational conditions of 7.8 mms^{-1} scanning speed, 12.91 $gmin^{-1}$ powder feed rate and 1675 W laser power. Similarly, Akinwande *et al*. [26] explored the impact of TiC reinforcement and laser power on the properties of CoCrFeMnNi HEAs. In this study, both laser power and TiC were varied.and the investigation identified an optimal entropy alloy mix of $(CoCrFeMnNi)_{85}/TiC_{15}$ at a laser power of 504 W, resulting in improved mechanical strength and hardness. The observed improvement was primarily

attributed to grain refinement induced by the reinforcing potential of the TiC particulte and the optimized thermal conditions during processing.

These findings have shown that RSM provides a framework for finding optimal process parameters that maximize specific response. Accordingly, this research adopts RSM as a statistical tool to optimize the laser processing parameters for the AlCrFeNiTiVZr HEA. The study aims to establish reliable correlations between predicted and experimental responses, thereby enhancing process efficiency and material performance.

2 Materials and methodology

2.1 Selection of materials

The chemical compositions of the AlCrFeNiTiVZr (HEA) powders used in the study are Al (Aluminum), Cr (Chromium), Fe (iron), Ni (Nickel), Ti (Titanium), V (Vanadium), and Zr (Zirconium) with equal weight percentage for each element. The powders were commercially supplied with a particle size that spanned 45 to 90 μm [27]. Bulk HEA samples with the AlCrFeNiTiVZr composition were fabricated on a 100 x 100 x 5 mm^3 mild steel substrate using an Optomec 850R LENS fiber laser system. The scanning speed for the laser parameters was maintained at 6.73 mm/s, while the laser power was varied between 300W and 380 W with increment of 20 W.

2.2 Experimental procedure and characterization of the powder

The cross-section of the fabricated samples was prepared using standard metallographic procedures in accordance with ASTM E3 standard [28]. The crystallographic structures of the laser deposited samples were examined using a Bruker D8 Advance X-ray diffractometer fortified with Cu Kα radiation (λ = 1.5406 Å), operating at a power of 40 kV and 30 mA. The diffraction patterns were analysed using the HighScore Plus software from Panalytical in conjunction with the 2021 ICCD data base for phase identification. Nanomechanical properties, including nanohardness and elastic modulus, were evaluated using an Anton-Paar TTX-NHT3 Nanoindenter with a spherical tip. Each indentation, including loading, holding, and unloading (20 seconds each), took 60 seconds to complete, with a maximum force of 400 mN applied during the nanoindentation studies. The elastic modulus values reported in this study were directly derived from these nanoindentation tests using the TTX-NHT3 system. The as-built samples were also subjected to dry sliding wear tests at 25 ^oC using a ball-on-disc rotating setup with a TRB3 Anton Paar Tribometer coupled to a S 128 surtronic profilometer. A steel ball of 6 mm diameter was used as the sliding counterface. The tests were carried out with an applied load of 20 N for 1000 sliding cycles. The attached surtronic profilometer was employed to measure the wear track depth and to investigate the coefficient of friction.

2.3 Statistical modelling of laser process parameters for AlCrFeNiTiVZr HEAs using response surface methodology (RSM)

The experiments were conducted on the as-built HEA samples, and the processing parameters were optimized. The data analysis and process optimization were conducted using Design-Expert 13.0.5.0 software (Stat-Ease Inc.). Based on the Design of Experiments (DOE) approach, five experimental runs were conducted using the CCD (central composite design) module under the framework of RSM (Response Surface Methodology). The build-up information for the model and the actual and coded controllable factors are presented in Tables 1 and 3, respectively. The number of experiments was determined using Equation (1) [29]:

$$N = 2k\,(\,k - 1) + Co \qquad (1)$$

Here, k signifies the count of independent variables, while C_0 represents the number of center points incorporated to estimate experimental error and ensure model robustness.

Table 1. Build statistics of the design for AlCrFeNiTiVZr HEA.

Specifications for the models	**Input value or description**
Software version	13.0.5.0
Study type	RSM
Number of runs	5.00
Blocks	Nil
Build Time (ms)	34
Sub-type	Randomized
Design specification	Central composite
Design Model	Quadratic

Table 2. Actual and coded controllable factors of the design for AlCrFeNiTiVZr HEA.

Factor	**Type**	**Subtype**	**Min.**	**Max.**	**Coded Low**	**Coded High**	**Mean**	**Std. Dev**
Laser Power (W)	Num.	Cont's	300	380	-1↔300	+1↔380	340	31.62
Scanning Speed (m/s)	Num.	Cont's	6.73	6.73	-1↔6.73	+1↔6.73	6.73	0.000

Table 3. Design of experiments (DOE).

Sample	**Run**	**Factor 1 A: Laser power (W)**	**Factor 2 B: Scanning speed (ms)**
T2	2	320	6.73
T1	3	300	6.73
T4	5	360	6.73
T3	1	340	6.73
T5	4	380	6.73

The system behaviour was described by a second-order quadratic polynomial model, which effectively captured the complex, nonlinear dependencies linking the laser processing parameters to the response outputs-nanohardness, wear resistance and elastic modulus, as indicated in Equations (2) and (3) [30]:

$$Y = \beta_o + \sum_{i=1}^{k} \beta_i A_i + \sum_{i=1}^{k} \beta_{ii} A_i^2 + \sum_{i=1}^{k} \beta_{ij} A_i B_{ij} + \mathbf{\mathcal{E}} \quad (2)$$

$$Y = \beta_o + \beta_i A_i + \beta_{ii} B_{ii} + \ldots + \beta_k A B_{ko} \quad (3)$$

The response output is denoted by Y, where β_0 represents the intercept constant, and the regression coefficients of the model are represented by β_i, β_{ii}, β_k and β_{ij}. The input variables, their corresponding squares and interaction terms are denoted by Ai, A_i^2 and A_iB_{ij}. The symbols o, i, ij, and ii are used to represent the regression coefficients that are not known, while the model's error is shown as Ɛ.

The transformation from Equation (2) to Equation (3) serves primarily to simplify the representation of the model for interpretative purposes. While Equation (2) explicitly expands all contributing terms, Equation (3) is a symbolic condensation used to generalize the polynomial structure of the model without listing each individual term. This transformation aids in readability and highlights the presence of linear, quadratic, and interaction effects without repeating the full functional form.

To build the regression model, the Central Composite Design (CCD) type in the Design Expert 13.0.5.0 software package was loaded for five experimental runs (see Table 3). The choice of CCD over other designs was motivated by its suitability for fitting second-order models, its ability to provide robust estimates of curvature, and its efficiency in minimizing the number of required experiments while maximizing information gain. The statistical validity of the model was confirmed through ANOVA (Analysis of Variance), which yielded a 95% confidence interval and p-values (probability values) less than 0.05. The soundness of the model was proven using ANOVA.

3 Results and discussions

3.1 Model validation and optimization of as-built AlCrFeNiTiVZr HEA

The measured results of nanohardness, elastic modulus, and wear for the as-built AlCrFeNiTiVZr HEA are presented in Table 4.

Table 4. Nanohardness, elastic modulus and wear measurement results.

Sample	Nanohardness (GPa)	Elastic Modulus (GPa)	Wear rate (X 10^{-4} mm^3/N/m)
T2(320 W)	0.98167	9.9587	3.6470
T1(300 W)	0.8317	8.8856	5.5250
T4(360 W)	1.3413	12.780	0.4258
T3(340 W)	1.2506	11.774	1.9080
T5(380 W)	2.0092	14.725	0.3525

The nanohardness values ranged from 0.8317 to 2.0092 GPa, while the elastic modulus values ranged from 8.8856 to 14.725 GPa. The low nanohardness and elastic modulus values may be attributed to microcracks, which disrupted the load transfer during testing and resulting in the HEA easy deformation under the indenter. The wear test results ranged from $3.525E^{-5}$ to $5.525E^{-4}$ mm^3/N/m. The ANOVA results with its key statistical tools are shown in Table 5, 'Cor.' refers to the corrected total sum of squares, 'Adeq.' represents adequate precision, a measure of the signal-to-noise ratio and 'R^2' denotes the coefficient of determination, indicating the amount of variance in the response described by the model.

Table 5: The ANOVA results with key statistical indicators for the developed model.

SOURCE	SS	DF	MS	F-VALUE	P-VALUE	STATISTICS
			Nanohardness			
Model	0.8252	2	0.4126	748.60	0.0013	Significant
A-Laser power	0.8084	1	0.8084	1466.76	0.0007	R^2 0.9987
B-Scan speed	0.0883	1	0.0883	160.14	0.0062	Adjusted R^2 0.9973
Residual	0.0011	2	0.0006			Predicted R^2 0.9806
Cor. total	0.8263	4				Adeq. Precision 63.6886
			Elastic Modulus			
Model	21.18	2	10.59	339.26	0.0029	Significant
A-Laser Power	20.96	1	20.96	671.30	0.0015	R^2 0.9971
B-Scan Speed	0.1594	1	0.1594	5.10	0.1524	Adjusted R^2 0.9941
Residual	0.0624	2	0.0312			Predicted R^2 0.8967
Cor. Total	21.25	4				Adeq. Precision 43.0865
			Wear rate			
Model	$1.961E^{-7}$	2	$9.805E^{-8}$	138.74	0.0072	Significant
A-Laser power	$1.627E^{-7}$	1	$1.627E^{-7}$	230.17	0.0043	R^2 0.9928
B-Scan speed	$1.068E^{-8}$	1	$1.068E^{-8}$	15.11	0.0603	Adjusted R^2 0.9857
Residual	$1.413E^{-9}$	2	$7.067E^{-9}$			Predicted R^2 0.8025
Cor. Total	$1.975E^{-7}$	4				Adeq. Precision 25.2292

The models for the three responses (nanohardness, elastic modulus, and wear rate) showed a linear fit that were statistically significant, with probability values of 0.0013, 0.0029, and 0.0072, respectively. The residual plot versus the run, illustrated in Figure 1, further demonstrates that the design remains within the process boundaries. For the model to be valid, the design plot should fall within the control margin [31]. It is evident from the plots presented in Figure 5 that the design points remain within the specified control boundaries (red lines); consequently, the models are deemed valid.

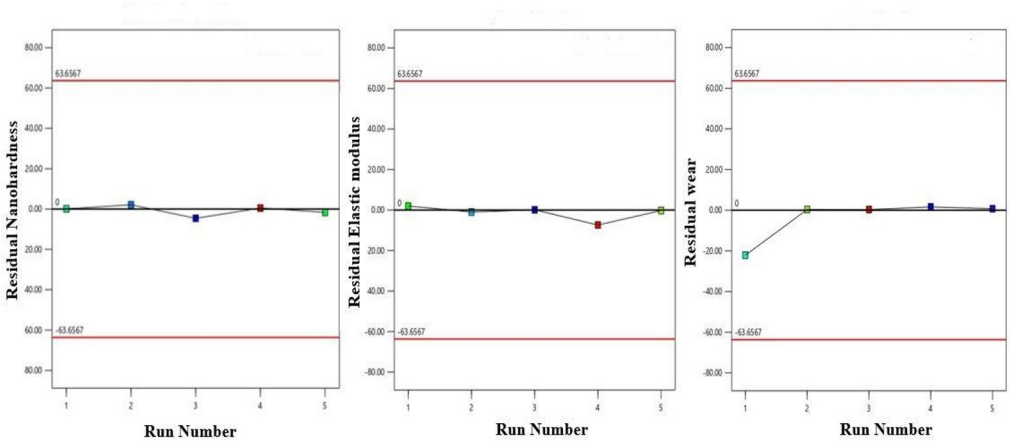

Fig. 1. Residual plots of nanohardness, elastic modulus and wear rate.

The following metrics were assessed in order to support the significance of the model and consistency using the ANOVA tool. For the nanohardness response, the R^2, Predicted R^2, and

Adjusted R^2 were 0.9987, 0.9806, and 0.9973, respectively. For the elastic modulus, the corresponding values were 0.9971, 0.8967, and 0.9941, while for the wear rate, they were 0.9928, 0.8025, and 0.9857, respectively. In all cases, the difference between the Predicted R^2 and Adjusted R^2 was less than 0.2, which indicates that the models exhibit good internal consistency and predictive reliability. This threshold serves as a practical benchmark, suggesting that the models are not overfitted and are capable of accurately predicting new response values within the design space. Additionally, the Adeq. Precision values (which assess the signal-to-noise ratio) were well greater than four thresholds, indicating the reliability in navigating the design space. The p-values for the nanohardness, elastic modulus, and wear rate were less than 0.05, suggesting that the models are statistically significant and the input responses and factors relationships are not random (Table 5). Furthermore, the Model F-values for the nanohardness, elastic modulus, and wear rate were 748.60, 339.26, and 138.74, respectively; also confirming the statistical significance of the models. The 3D-surface interaction plots in Figure 2 describe the 3D response surface plots showing the influence of the process parameters on each response variable.

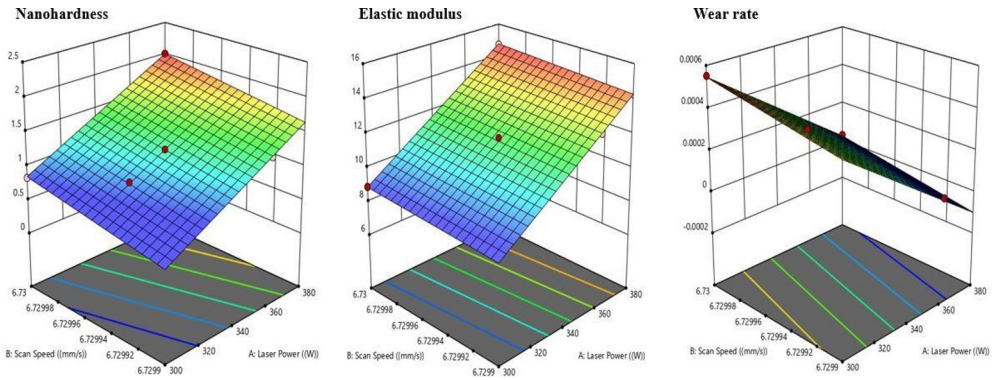

Fig. 2. 3D response surface plots of operating parameters on the corresponding responses-nanohardness, elastic modulus and wear rate.

Based on the coded factors, the final model equations of responses, are as follow:

$$\text{Nanohardness} = +1.25 + 0.5791 \times A + 0.1808 \times B \quad (4)$$

$$\text{Elastic modulus} = +11.58 + 2.95 \times A + 0.2429 \times B \quad (5)$$

$$\text{Wear rate} = +0.0002 - 0.0003 \times A + 0.0.0001 \times B \quad (6)$$

Where A and B represent the coded values of laser power and scan speed respectively.

Using the actual factors, the final model equations of responses, are as follow:

$$\text{Nanohardness} = -24339.63 + 0.0145 \times p + 3616.067 \times v \quad (7)$$

$$\text{Elastic modulus} = -32713.566 + 0.0737 \times p + 4858.889 \times v \quad (8)$$

$$\text{Wear rate} = -8.462 - 6.494E^{-06} \times p + 1.2578 \times v \quad (9)$$

Here, p signifies the laser power (W) and v denotes the scan speed (mm/s).

To further assess the effect of the processing parameters on the output responses, including nanohardness, elastic modulus, and wear rate characteristics, contour plots were

generated from the regression models, as shown in Figure 3 [32-37]. The lower responses are indicated by the blue colors, while the higher responses are represented by the red colors. The most influential parameter combination was a laser power of 380 W and a scan speed of 6.73 mm/s, which could produce the desirable responses of 2.0092 GPa, 14.725 GPa and 5.525×10^{-4} mm³/N/m for nanohardness, elastic modulus, and a wear rate respectively, from a possible set of nine experimental runs. It could be noticed that the nanohardness, elastic modulus, and wear resistance increased with an increase in laser power at a constant scan speed, highlighting the importance of microstructural integrity.

The X-Ray Diffraction (XRD) patterns showing the crystal structure of the laser-deposited AlCrFeNiTiVZr high-entropy alloy are presented in Figure 4. The results reveal an increase in peak intensities with the same trend; consistent phases and increased intensities observed for all samples. This suggests that the phase dominance is Body Centered Cubic (BCC) solid solution and there is an improvement in crystallinity of the BCC phase due to enhances atomic ordering. Samples T1 (300W) and T2 (320W) showed peaks that are broader than the rest which may suggest that there are smaller crystallite sizes which can be attributed to the rapid solidification at 300 and 320 W. As laser power increased, the gradual disappearance of secondary BCC (BCC2) peaks in samples T3 (340 W) to T5 (380 W) suggests a phase transformation from BCC2 to a more dominant BCC1 phase, likely due to higher thermal input and extended diffusion times. This indicates that increasing laser power promotes phase stability and the refinement of the HEA microstructure. The prominent diffraction peaks occurred at 2θ values of approximately 31.5°, 36°, 42.5°, 49.5°, 58.5°, and 66°, corresponding to (hkl) planes of (110), (200), (211), (220), (310), and (222), respectively.

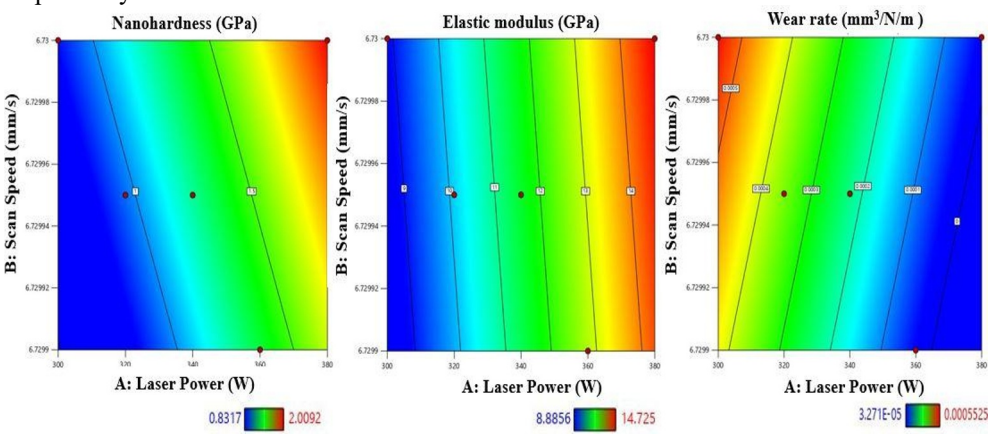

Fig. 3. Contour plots of operating parameters on the corresponding responses-nanohardness, elastic modulus and wear rate.

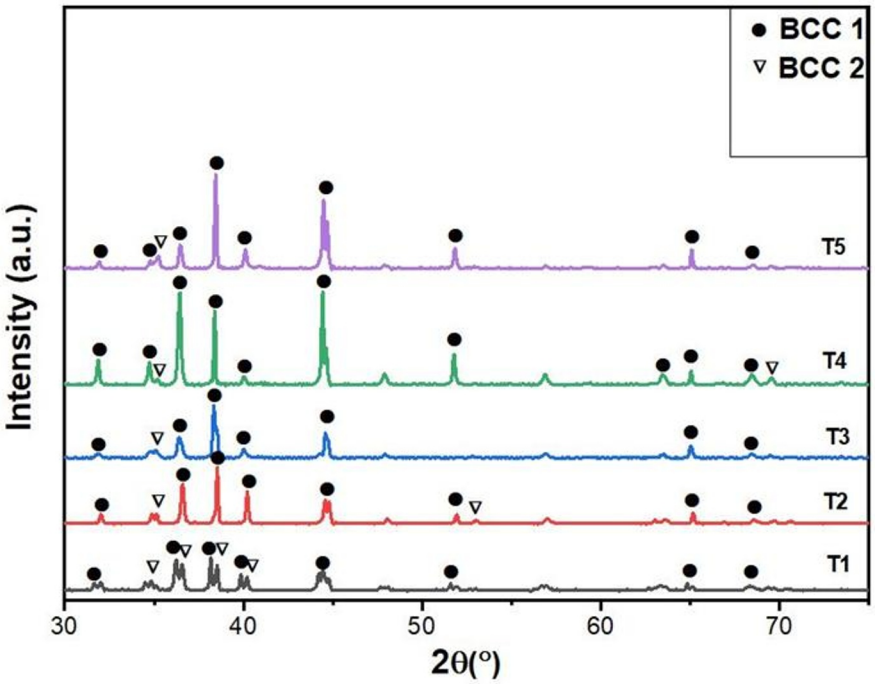

Fig. 4. XRD pattern of as-built AlCrFeNiTiVZr HEA.

4 Conclusion

In this investigation, laser power was varied during the fabrication of High-Entropy Alloys AlCrFeNiTiVZr (HEAs). The deductions drawn from this are as follow:

1. Crystallographic analysis confirmed that the dominant phase of the HEAs is the BCC, showing the HEAs formed solid solution structures
2. Nanomechanical testing confirmed that higher laser power improved hardness and wear resistance. Sample T5 exhibited the highest hardness (2.0092 GPa).
3. The elastic modulus results showed a direct proportionality, where optimized laser power (above 340 W) significantly enhanced these properties.
4. Generally, laser power in the range of 340–380 W was identified as optimal for achieving a balance of hardness, wear resistance, and elasticity, providing a foundation for developing high-performance materials for various applications. Nonetheless, more work is needed to optimize the microstructures of the HEAs to be crack free which will significantly enhance the mechanical performance of the HEAs.

The statistical analysis of the developed regression model, including the P-value, F-value, Predicted R^2, Adjusted R^2. Adequate Precision values further supported the model's robustness and predictive reliability. The close alignment between experimental and predicted outcomes confirmed the model's precision. This study underscores the critical importance of meticulously controlling the processing parameters, particularly laser power, to precisely engineer the microstructure and, consequently, the resulting mechanical performances of these advanced AlCrFeNiTiVZr high-entropy alloys. This custom-made approach is crucial for optimizing the functionality of these materials in demanding

applications. The robust predictive model, validated through the comprehensive statistical evaluation, provides a reliable framework for understanding the relationships between the processing conditions and the microstructural evolution, as well as the associated mechanical characteristics of the AlCrFeNiTiVZr high-entropy alloys. This knowledge can assist in creating advanced materials that possess specific characteristics suitable for diverse industrial and technological applications.

References

[1] S. Wei, F. He, C. C. Tasan, Metastability in high-entropy alloys: A review. J. Mater. Res. **33**, 2924-2937 (2018) https://doi.org/10.1557/jmr.2018.306
[2] J.-T. Ren, L. Chen, H.-Y. Wang, Z.-Y. Yuan, High-entropy alloys in electrocatalysis: from fundamentals to applications. Chem. Soc. Rev. **52**, 8319-8373 (2023) https://doi.org/10.1039/d3cs00557
[3] X. Wang, W. Guo, Y. Fu, High-entropy alloys: emerging materials for advanced functional applications. J Mater. Chem. A. **9**, 663-701 (2021) https://doi.org/10.1039/d0ta09601F
[4] Behera, Advanced Materials: An Introduction to Modern Materials Science, (Springer, 2021)
[5] P. A. Ibrahim, İ. Özkul, C. A. Canbay, An overview of high-entropy alloys. Emerg. Mater. **5**, 1779-1796 (2022). https://doi.org/10.1007/s42247-022-00349-z
[6] J.-T. Ren, L. Chen, H.-Y. Wang, Z.-Y. Yuan, High-entropy alloys in electrocatalysis: from fundamentals to applications. Chem. Soc. Rev. **52**, 8319-8373 (2023). https://doi.org/10.1039/d3cs00557G
[7] A. M. Oketola, T. A. Adegbola, T. Jamiru, O. Ogunbiyi, S. Salifu, Advances in High-Entropy Alloy Research: Unraveling Fabrication Techniques, Microstructural Transformations, and Mechanical Properties. J. Bio Tribo Corros. **11**, 79 (2025). https://doi.org/10.1007/s40735-025-00999-6
[8] S.S. Nene, High Entropy Alloys, (Singapore: Springer Nature Singapore, 2024). https://doi.org/10.1007/978-981-99-7173-2
[9] C. Han, Q. Fang, Y. Shi, S.B. Tor, C.K. Chua, K. Zhou, Recent advances on high-entropy alloys for 3D printing. Adv. Mater. **32**, 1903855 (2020). https://doi.org/10.1002/adma.201903855
[10] Kunce, M. Polanski, J. Bystrzycki, Structure and hydrogen storage properties of a high entropy ZrTiVCrFeNi alloy synthesized using Laser Engineered Net Shaping (LENS). Int. J. Hydrog. Energy. **38**, 12180–12189 (2013). https://doi.org/10.1016/j.ijhydene.2013.05.071
[11] L. Zhou, J. Miller, J. Vezza, M. Mayster, M. Raffay, Q. Justice, Additive manufacturing: a comprehensive review. Sens. **24**, 2668 (2024). https://doi.org/10.3390/s24092668
[12] J. O. Milewski, Additive manufacturing of metals: from fundamental technology to rocket nozzles, medical implants, and custom Jewelry, (Springer, 2017). https://doi.org/10.1007/978-3-319-58205-4_2
[13] K. Carpenter, A. Tabei, On residual stress development, prevention, and compensation in metal additive manufacturing. Mater. **13**, 255 (2020). https://doi.org/10.3390/ma13020255
[14] N. Bastola, M. P. Jahan, N. Rangasamy, C. S. Rakurty, A review of the residual stress generation in metal additive manufacturing: analysis of cause, measurement, effects, and prevention. Micromachines (Basel). **14**, 1480 (2023).

https://doi.org/10.3390/mi14071480
[15] B. He, C. Bi, X. Li, W. Wang, G. Yang, Residual stresses and deformations of laser additive manufactured metal parts: a review. Int. J. Mater. Form. **16**, 7 (2023). https://doi.org/10.1007/s12289-022-01729-w
[16] S. G Jeong, G. M. Karthik, E. S. Kim, A. Zargaran, S. Y. Ahn, M. J. Sagong, Architectured heterogeneous alloys with selective laser melting. Scr. Mater. **208**, 114332 (2022). https://doi.org/10.1016/j.scriptamat.2021.114332
[17] J. Huang, W. Yang, Z. Gao, X. Hou, X.-S. Yang, Heterostructured multi-principal element alloys prepared by laser-based techniques. Microstr. **5**, (2025). http://dx.doi.org/10.20517/microstructures.2024.86
[18] J. Gao, X. Wang, C. Wang, Y. Hao, X. Liang, W. Li, K. Zhao, Multi-objective optimization of process parameters for laser metal deposition of NiTi shape memory alloy based on neural network and genetic algorithm. J. Adv. Manuf. Technol. **130,** 4663-4678 (2024). https://doi.org/10.1007/s00170-024-12974-5
[19] X. Wu, G. Zhou, D. Sun, L. Chen, J. He, S. Wang, F. Xie, Cultivating a comprehensive understanding of microstructural attributes and wear mechanisms in FeCrCoNiAlTix high-entropy alloy coatings on TC6 substrates through laser cladding fabrication. J. Alloys Compd. **984**, 173865 (2024). https://doi.org/10.1016/j.jallcom.2024.173865
[20] M. Zhang, Y. Wang, Y. Zhou, D. Wang, X. Yang, D. Wang, G. Zhang, Surface morphology evolution and tribological properties of laser directed energy deposited CoCrFeNi high-entropy alloys using laser polishing. J. Alloys Compd. **1022**, 179893 (2025). https://doi.org/10.1016/j.jallcom.2025.179893
[21] M. Dada, P. Popoola, O. Aramide, N. Mathe, S. Pityana, Optimization of the corrosion property of a high entropy alloy using response surface methodology. Materials Today: Proceedings, **38,** 1024-1030 (2021). https://doi.org/10.1016/j.matpr.2020.05.618
[22] D. Shao, X. Bi, M. Hong, R. Li, Optimization of Process Parameters for Laser-Directed Energy Deposition Coatings of FeCoNi+ 1% Y_2O_3 High-Entropy Alloy Based on Response Surface Methodology. Mater. **18**, 883 (2025). https://doi.org/10.3390/ma18040883
[23] S. Lamidi, N. Olaleye, Y. Bankole, A. Obalola, E. Aribike, I. Adigun, Applications of response surface methodology (RSM) in product design, development, and process optimization. IntechOpen, (2024). https://doi.org/10.5772/intechopen.106763
[24] A. A. Siddiqui, A. Dubey, C. Paul, Geometrical characteristics in laser surface alloying of a high-entropy alloy. Lasers in Engr. **43**, 237-259 (2019)
[25] Z. Dong, L. Feng, H. Long, B. Lu, J. Zhu, X. Yan, R. Ma, C. Qiu, Y. Gui, M. Liu, A multi-objective optimization of laser cladding processing parameters of $AlCoCrFeNi_{2.1}$ eutectic high-entropy alloy coating. Opt. Laser Technol. **170**, (2024). https://doi.org/10.1016/j.optlastec.2023.110302
[26] A.A. Akinwande, O.A. Balogun, A.A. Adediran, O.S. Adesina, V. Romanovski, T.C. Jen, Experimental analysis, statistical modeling, and parametric optimization of quinary-(CoCrFeMnNi) 100–x/TiCx high-entropy-alloy (HEA) manufactured by laser additive manufacturing. Results Eng. **17**, 2 (2023). https://doi.org/10.1016/j.rineng.2022.100802

[27] L. Kanyane, P. Lepele, N. Malatji, M. Shongwe, 3D finite element analysis and experimental correlations of laser synthesized AlCrNiTiNb high entropy alloy coating. Mater. Today Commun. **38**, 107686 (2024). https://doi.org/10.1016/j.mtcomm.2023.107686
[28] D.W. Hetzner, Microindentation hardness testing of materials using ASTM E384. Microsc. Microanal. **9**, 708-709 (2003)
[29] O. Ogunbiyi, T. Jamiru, R. Sadiku, O. Adesina, J.L Olajide, L. Beneke, Optimization of spark plasma sintering parameters of inconel 738LC alloy using response surface methodology (RSM). Int. J. Lightweight Mater. Manuf. **3**, 177-188 (2020). https://doi.org/10.1016/j.ijlmm.2019.10.002
[30] L. Paul, S.S. Hiremath, Response surface modelling of micro holes in electrochemical discharge machining process. Procedia Eng. **64**, 1395-1404 (2013). https://doi.org/10.1016/j.proeng.2013.09.221
[31] E. Olorundaisi, B.J. Babalola, B.L. Bayode, L. Teffo, and P.A. Olubambi, Optimization of process parameters for the development of Ni–Al-Ti-Mn-Co-Fe–Cr high entropy alloy system via spark plasma sintering. J. Adv. Manuf. Technol. **126**, 3323-3337 (2023). https://doi.org/10.1007/s00170-023-11311-6
[32] A. Kumar, A. Singh, A. Suhane, Mechanically alloyed high entropy alloys: existing challenges and opportunities. J. Mater. Res. Technol. **17**, 2431-2456 (2022) https://doi.org/10.1016/j.jmrt.2022.01.141
[33] L. Deng, C.Y. Bai, Z.T. Jiang, J.R. Luo, J. Tu, H.Y. Xu, H. Huang, L. Tan, L.P. Ding, Effect of B4C particles addition on microstructure and mechanical properties of $Fe_{50}Mn_{30}Co_{10}Cr_{10}$ high-entropy alloy. Mater. Sci. Engr. **822**, 1041642 (2021). https://doi.org/10.1016/j.msea.2021.141642
[34] S.G. Ma, Y. Zhang, Effect of Nb addition on the microstructure and properties of AlCoCrFeNi high-entropy alloy. Mater. Sci. Engr. **532**, 480-486 (2012). https://doi.org/10.1016/j.msea.2011.10.110
[35] H. Wu, S. Huang, H. Zhu, Z. Xie, Strengthening FeCrNiCu high entropy alloys via combining V additions with in-situ TiC particles. Scr. Mater. **195**, 113724 (2021). https://doi.org/10.1016/j.scriptamat.2021.113724
[36] H. Wu, S. Huang, H. Qiu, H. Zhu, Z. Xie, Effect of Si and C additions on the reaction mechanism and mechanical properties of FeCrNiCu high entropy alloy. Sci. Rep. **9**, 16356 (2019). https://doi.org/10.1038/s41598-019-52809-y
[37] D.H. Lee, J.M. Park, G. Yang, J. He, Z. Lu, J.Y. Suh, M. Kawasaki, U. Ramamurty, J.I. Jang, Nano-graining a particle-strengthened high-entropy alloy. Scr. Mater. **163**, 24-28 (2019). https://doi.org/10.1016/j.scriptamat.2018.12.033